From Paper to Paper-like Hierarchical Anatase TiO2 Film Electrode for High-Performance Lithium-Ion Batteries

2 AUTHORS:

Bote Zhao
Georgia Institute of Technology
29 PUBLICATIONS **371** CITATIONS

SEE PROFILE

Zongping Shao
Nanjing University of Technology
**423** PUBLICATIONS **10,438** CITATIONS

SEE PROFILE

From Paper to Paper-like Hierarchical Anatase TiO₂ Film Electrode for High-Performance Lithium-Ion Batteries

Bote Zhao and Zongping Shao*

State Key Laboratory of Materials-Oriented Chemical Engineering, College of Chemistry & Chemical Engineering, Nanjing University of Technology, No. 5 Xin Mofan Road, Nanjing 210009, P. R. China

ABSTRACT: A paper-like self-standing film electrode composed of hierarchical mesoporous anatase TiO₂ was designed and prepared through a facile route of filter paper templating in combination with an additional deep hydrolysis treatment process. The specific surface area of hierarchical mesoporous TiO₂ increased to 155.6 m² g⁻¹ compared to the sample without the additional deep hydrolysis, which is only 16.0 m² g⁻¹. The results are consistent with a simple model of sphere stacking which suggests that the rich mesopores were from the void space created by the TiO₂ stacking. By applying such film as binder-free electrode in lithium-ion batteries (LIBs), good rate performance was demonstrated, and the capacity was still 100 mA h g⁻¹ even at the high rate of 20 C. The contributions of Li⁺ insertion/extraction reaction and capacitive effect on the capacities were investigated by cyclic voltammetry and calculation. With the sweep rate increased from 0.1 to 10 mV s⁻¹, the contributions of capacitive effects increased from 46% to 88% of the total capacities. The uniquely architectural TiO₂ film electrode showed excellent cycling performance at high rate of 10 C through 400 cycles. It highly promises as a new anode for thin-film batteries with versatile application fields.
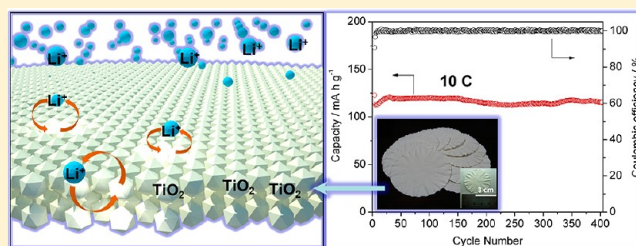
◼ INTRODUCTION

Environmental pollution and energy crisis constrain sustainable development of our economy and modern society. One way to potentially solve those problems is the utilization of alternative clean energy sources and electric motors for replacement of the widely used fossil fuels and internal combustion engines, respectively. Lithium-ion batteries (LIBs), which are electrochemical energy storage devices based on lithium-ion conducting electrolyte with the energy stored in the lithium-intercalation electrode materials, have been extensively applied in personal electronics sector with great success in the past decade. Recently, it is generally accepted that LIBs may also play important role in our future clean energy system, as attracted by their high voltage, no memory effect, high energy density, and environmental benignity.[1] For example, LIBs can perform as electrochemical energy storage for new energy sources like solar, wind, waves, and even nuclear as well as power sources for electric vehicles (EVs) and hybrid electric vehicles (HEVs) to realize zero emission during the utilization of energy.

Conventional LIBs with graphite/carbon anode, which are designed mainly as power sources for portable electronic devices, however, suffer from poor safety at fast discharge rate, thus making them unsuitable for large scale application. The poor safety is originated from the low intercalation potential of lithium at around 0.1 V vs Li/Li⁺ for graphite/carbon anode. At fast discharge rate, the electrode is easily polarized to such a degree that dendritic lithium may be formed over the anode surface, which can penetrate the porous separator to introduce the risk of internal circuit shortage as well as combustion/

explosion. In order to realize their practical application in those new emerging fields, alternative LIBs with improved safety, high volumetric/gravimetric energy density, and high charge/discharge rate performance have to be developed.

TiO₂ is a promising anode material of LIBs, which can intercalate lithium ion at 1.0−3.0 V vs Li/Li⁺;[2−4] such high potential can effectively avoid the formation of solid electrolyte interface and dendritic lithium over the anode surface, ensuring a good safety. Among the various polymorphs of TiO₂, anatase, which allows 3D lithium intercalation, is the most suitable structure to perform as a lithium-intercalation host. The reaction of lithium insertion into TiO₂ can be written as TiO₂ + xLi⁺ + xe⁻ = Li$_x$TiO₂. One mole of lithium may be intercalated per molecular TiO₂ to give a theoretical capacity of 336 mA h g⁻¹, which is comparable to that of graphite. However, TiO₂ suffers from low lithium ion and electron conductivity, which limits the rate capacity of electrode made from coarse TiO₂.

Nanostructuring is considered to be an effective way in improving rate performance of LIBs by effectively reducing transport distance for both electron and lithium ion during the electrochemical reaction process.[5,6] The templating technique is versatile to construct advanced nanostructured materials with controllable size, structures, and desirable functions.[7−10] Through templating synthesis, nanostructured electrode materials with different morphologies from 0D particles to

3D porous architectures can be developed. Outstanding electrochemical performance has been reported by applying those template-synthesized materials as electrodes.[11] Binder- and conductive additive-free hierarchical porous films may also be prepared by proper templating synthesis. To perform as electrodes of LIBs, such films show several outstanding advantages over conventional electrodes, such as lighter weight, higher energy density, and better cycling stability. So far, a wide range of materials have been employed as templates, such as anodic aluminum oxide, silica, organic surfactants, polymers, and even biological viruses.[12−19] Brezesinski et al. synthesized mesoporous TiO_2 film for high performance electrochemical energy storage by the templating method. However, the preparation procedure of the template they used (KLE-type block copolymers) is complicated.[18] Cost is still a big issue that prevents the templating technique for wide application. It is critical to find a template that is low cost, facile operation, and easy elimination. Cellulose fibers are natural porous substance, which have attracted attention as templates for the fabrication of powders and nanotubes for functional applications because of their low cost, abundance, and easy elimination through burning.[20−22] More interestingly, cellulose fibers can be easily formed into films, which can then be applied as sacrificing templates to prepare functional films for various applications. For example, filter papers and cotton clothes have been successfully applied as templates for fabricating ZnO film for gas sensing and for preparing MoO_2 film electrode for LIBs, respectively.[23,24] However, because of low specific surface area of conventional cellulose fibers, it is typically difficult to introduce sufficient micropores and mesopores into the samples, which are important to improve the electrochemical performance of the materials as electrodes of LIBs by increasing the interfacial reaction area and shortening the diffusion distance for both electron and lithium ion.

Herein, we reported a facile way for fabricating hierarchical mesoporous anatase TiO_2 films with high specific surface area as anodes of LIBs by using easily accessible cellulose filter papers as template together with a following deep hydrolysis treatment in boiling water, as shown in Figure 1. The filter papers templating allowed the creation of a film-type TiO_2 skeleton, while the deep hydrolysis process significantly increased mesopores in the film electrode by reconstructing TiO_2 at microdomain. The as-fabricated TiO_2 paper-like films were then applied directly as a binder-free electrode for LIBs, showing outstanding electrochemical performance.

■ EXPERIMENTAL SECTION

Fabrication of Thin Film. Filter papers (quantitative #203, Hangzhou Xinhua Paper Industry Co., Ltd., China) were used as received without further treatment. In a typical process, 100 mL of ethanol, 10 mL of acetic acid, and 30 g of tetrbutyl titanate ($C_{16}H_{36}O_4Ti$) were added into a beaker and stirred until a homogeneous solution was obtained. Ten pieces of filter papers were immersed into the solution, followed by stirring for 2 h at room temperature. The solution on the surface of filter paper was removed by tissue papers. Then the filter papers were dried at 60 °C overnight and calcined at 450 °C in air for 2 h with a heating rate of 2 °C min^{-1}. The impregnated filter papers were held between two planes of glass in a fixed gap during the calcination to keep the as-fabricated films in flat shape. The as-fabricated TiO_2 thin film was named TiO_2-0. The hierarchical TiO_2 thin film was obtained under the similar process but with an additional hydrolysis treatment. Briefly, after impregnation for 2 h, filter papers were hydrolyzed in deionized water for 3 h at 95−100 °C. Then the filter papers were dried at 60 °C overnight and calcined at 450 °C in air for 2 h with a heating rate of 2 °C min^{-1}. The as-fabricated hierarchical mesoporous TiO_2 thin film was named TiO_2-h.

Basic Characterization. The phase compositions of samples were determined at room temperature by X-ray diffraction (XRD, Bruker D8 advance diffractometer). Cu Kα radiation was used as an X-ray source. The morphologies of samples were observed by environmental scanning electronic microscope (ESEM, QUANTA-200) and transmission electron microscopy (TEM, JEOL JEM-2100). Prior to TEM analysis, the samples were prepared by ultrasonically suspending a piece of TiO_2 film in ethanol for several hours. A drop of the suspension was then applied onto holey carbon-coated copper grids and dried in air. The step was repeated for several times to ensure the specimens have been mounted on the copper grids. Nitrogen adsorption−desorption isotherms of samples were measured at 77 K using a TriStar II 3020 instrument. The specific surface area was obtained by the Brunauer−Emmett− Teller (BET) method. The pore size distributions were calculated applying the Barrett−Joyner−Halenda (BJH) method on the basis of the desorption branches of the isotherms.

Electrochemical Measurement. The electrochemical measurements of as-fabricated TiO_2 thin films were conducted with CR2016-type coin cells, which were assembled in an argon-filled glovebox. The TiO_2 thin films were cut into disk- shape film with a punch. The disk-shape film was transferred onto the current collector by a special spoon and used directly as the working electrode without any binder or conductive additive applied. The weight of the active material is about 1.5− 2 mg cm^{-2}. The copper foil with rough surface was used as current collector by only physical contact with the working electrode. The rough surface of copper foil was prepared by coating a silver paste layer on it and heat-treating under H_2/Ar at 300 °C for 1 h.[25] Metallic lithium was used as the counter electrode for all of the electrochemical measurements with a liquid electrolyte of 1 M $LiPF_6$ in a 1:1 (by volume) ethylene carbonate and dimethyl carbonate mixture. Microporous polypropylene film (Celgard, 2400) was used as the separator.
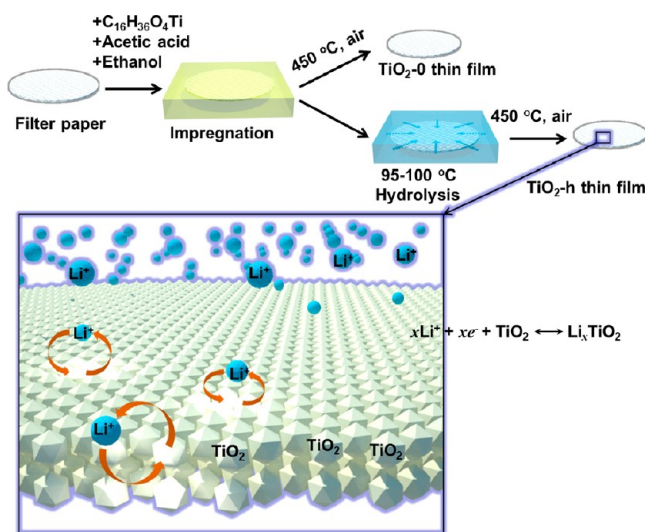

Figure 1. Fabrication process of paper-like TiO_2-0 and TiO_2-h thin films.

Electrochemical testing was completed under a constant current mode using a NEWARE BTS computer-controlled galvanostat (Shenzhen, China) between 1.0 and 3.0 V at room temperature. Cyclic voltammetry tests were performed over the potential range of 1.0–3.0 V using a Princeton Applied Research potentiostat/galvanostat model 273A at the sweep rates of 0.1–10 mV s^{-1}. Before tests of cyclic voltammogram (CV), rate performance, cycling performance, cells were activated for several cycles at 0.5 C.

RESULTS AND DISCUSSION

Fabrication of Hierarchical Mesoporous TiO$_2$ Paper-like Film. Cellulose with the formula $(C_6H_{10}O_5)_n$ is one of the most abundant natural organic substance. About 33% of all plant matter is cellulose; in particular, the cellulose content of cotton and wood reaches as high as 90% and 40–50%, respectively. On the other hand, papermaking technology has a very long history, which was invented at least 1900 years ago. Nowadays, papermaking has become a very mature and low-cost technology. In this study, we used disk-shape quantitative filter papers with diameters of around 7 cm as low-cost templates for the preparation of TiO$_2$ thin films (Figure 2a).
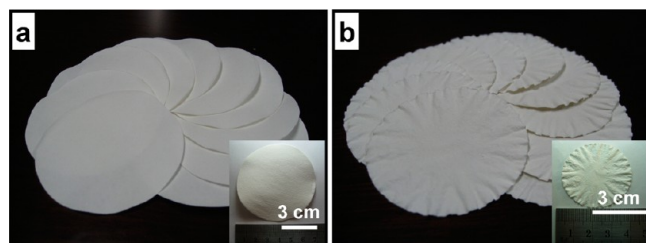

Figure 2. Digital photos of (a) filter papers and (b) as-fabricated TiO$_2$ thin films.

They were immersed in a solution composed of 100 mL of ethanol, 10 mL of acetic acid, and 30 g of tetrbutyl titanate (C$_{16}$H$_{36}$O$_4$Ti), as shown in Figure 1. After the impregnation for 2 h, the filter papers were picked out, and the liquid on the surface was removed by tissue papers. After drying at 60 °C overnight, the impregnated filter papers were calcined at 450 °C in air for 2 h to result in TiO$_2$ thin films (Figure 2b). From a macroscopic view, the as-fabricated TiO$_2$ films (named TiO$_2$-0) took after filter papers in morphologic shape, but the diameter reduced significantly to about 3.7 cm. White color of the films after the calcination suggests their carbon-free nature. We also conducted a deep hydrolysis treatment in boiling water of the dried filter papers after the impregnation with C$_{16}$H$_{36}$O$_4$Ti. The corresponding TiO$_2$ films after the calcination were named TiO$_2$-h. Obviously, it is a very facile and low-cost method for preparing paper-like thin films, with easy scale-up for commercial application.

Figure 3a,b shows typical SEM images of the filter papers before and after the impregnation with C$_{16}$H$_{36}$O$_4$Ti. The filter papers were constructed mainly from belt-shape cellulose fibers with width of 5–30 μm which were randomly stacked to nonwoven films, although some belts with much narrower width were also observed (Figure 3a). The filter papers are applied as skeletons for formation of paper-like TiO$_2$ film since the specific surface area of filter papers used here is as low as 1.3 m^2 g^{-1} obtained by the BET method. After the impregnation with C$_{16}$H$_{36}$O$_4$Ti, the filter papers showed similar morphology to the original ones, and no obvious swelled cellulose fibers
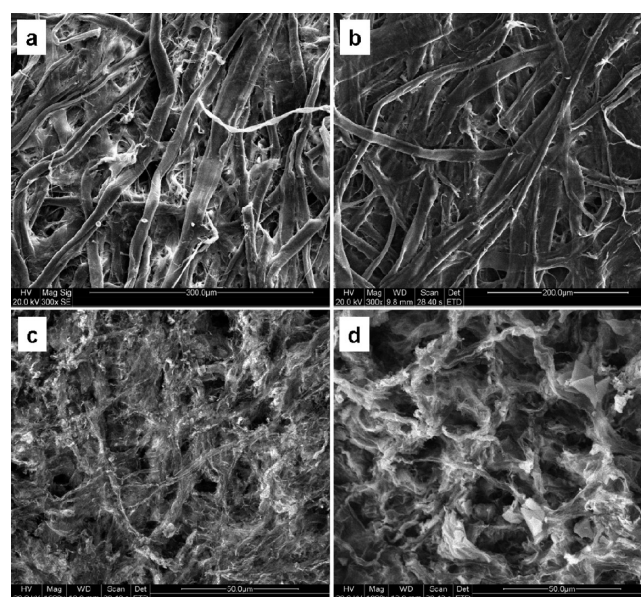

Figure 3. SEM images of (a, b) surfaces of filter paper before and after impregnation, (c) surface of TiO$_2$-0 film, and (d) surface of TiO$_2$-h film.

were observed (Figure 3b); however, the contrasting color of the films from the background became dark, suggesting the successful absorption of the C$_{16}$H$_{36}$O$_4$Ti into the filter papers. As a polysaccharide consisting of a linear chain of several hundred to over ten thousand $\beta(1{\rightarrow}4)$ linked D-glucose units, cellulose is rich in $-$OH and $-$C$-$O$-$C$-$ groups, which can easily coordinate with Ti ion to firmly anchor it on the cellulose surface; thus, the filter papers can be easily replicated by C$_{16}$H$_{36}$O$_4$Ti. The weight and thickness of the TiO$_2$ thin films can be controlled by tailoring the concentration of the C$_{16}$H$_{36}$O$_4$Ti solution for the impregnation. In this study, a high C$_{16}$H$_{36}$O$_4$Ti concentration was used for high TiO$_2$ yield per filter paper. As shown in Figure 3b, a considerable amount of C$_{16}$H$_{36}$O$_4$Ti was also located at the void space of belts. The typical SEM images of as-prepared TiO$_2$ films after the elimination of filter papers template by burning are shown in Figure 3c,d. Both TiO$_2$-0 and TiO$_2$-h samples can be treated as replica of filter papers. However, it seems that the samples after the calcination were composed of randomly and loosely packed fibers with width much smaller than the original cellulose belts. No significant difference in microstructure between TiO$_2$-0 and TiO$_2$-h was observed.

XRD patterns of the as-fabricated TiO$_2$-0 and TiO$_2$-h films are shown in Figure 4. The main diffraction peaks of both samples can be indexed well to anatase TiO$_2$ phase, corresponding to JCPDS, No. 21-1272, although a trace amount of brookite phase TiO$_2$ was also detected. The diffraction peaks of TiO$_2$-h phase were broader than that of TiO$_2$-0, suggesting the deep hydrolysis process during the synthesis effectively reduced the crystalline size of TiO$_2$. The average crystalline grain size of TiO$_2$-h analyzed based on the half-width of (101) peak via the Scherrer equation was estimated to be around 9.5 nm, while it was 18.9 nm for TiO$_2$-0 sample.

TEM observation was also conducted on both TiO$_2$-0 and TiO$_2$-h samples to get further information about their particulate morphology and grain size with the typical TEM and HR-TEM images presented in Figure 5. Both samples
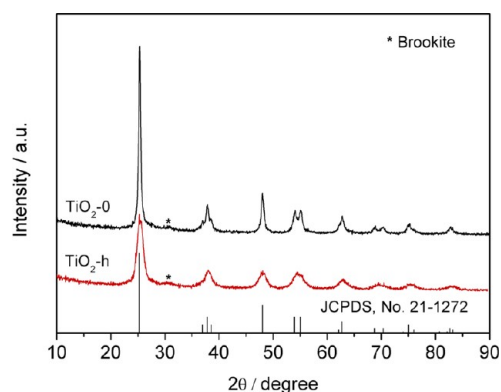
17442

dx.doi.org/10.1021/jp305744c | J. Phys. Chem. C 2012, 116, 17440−17447

Figure 4. XRD patterns of TiO$_2$-0 and TiO$_2$-h after calcination.
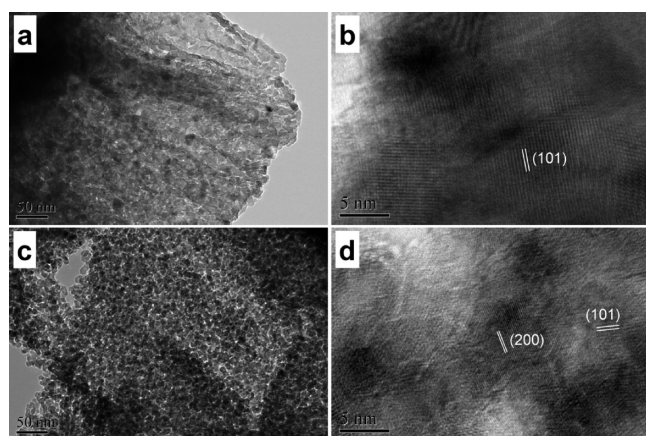

Figure 5. (a, c) TEM and (b, d) HR-TEM images of TiO$_2$-0 (a, b) and TiO$_2$-h (c, d).

showed thin sheet morphological structures. TiO$_2$-0 was composed of primary particles with the size of 15−20 nm, which were badly aggregated and sintered to well-densified particles (Figure 5a,b). Lattice fringe with an interplanar spacing of d = 0.34 nm was demonstrated in the HR-TEM image of TiO$_2$-0 as shown in Figure 5b, which well corresponds to the diffraction plane of (101) of anatase TiO$_2$. It suggests the main phase in TiO$_2$-0 is anatase TiO$_2$, in well agreement with the XRD results. Similar to TiO$_2$-0, TiO$_2$-h sample also showed a thin TiO$_2$ sheet structure for the secondary particles (Figure 5c), which demonstrated a very clear hierarchical structure and was composed of nanosized ultrafine primary particles with the size of 8−13 nm. Mesopores in TiO$_2$-h were distinctly demonstrated by TEM, which were further confirmed by HR-TEM as shown in Figure 5d. The interplanar spacings of d = 0.34 nm and d = 0.19 nm were also observed from Figure 5d, which can be related to the diffraction planes of (101) and (200) of anatase TiO$_2$, indicating the TiO$_2$ phase in TiO$_2$-h sample also took an anatase phase structure, in well agreement with the XRD results. Above results demonstrated that the deep hydrolysis treatment just altered the morphological structure, but it did not affect the basic phase structure of TiO$_2$.

To get further information about their microstructure, nitrogen adsorption−desorption isotherms of filter papers and TiO$_2$ samples were also measured with the results shown in Figure 6. There was no mesopore observed in the filter papers which had a very low BET surface area of 1.3 m^2 g^{-1}. TiO$_2$-h had a BET surface area as high as 155.6 m^2 g^{-1}, and its isotherm curve can be attributed to typical type IV and demonstrated
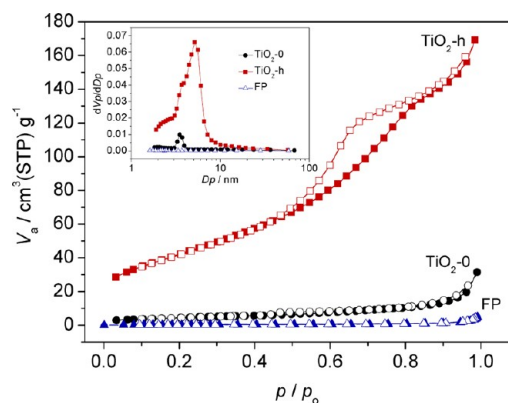

Figure 6. Nitrogen adsorption−desorption isotherms of TiO$_2$-0, TiO$_2$-h, and filter papers (FP) (inset: BJH pore size distribution plots).

distinct hysteresis loop, suggesting the presence of mesopores. According to the Barrett−Joyner−Halenda (BJH) pore size distribution plot as shown in the inset of Figure 6, the pore size of TiO$_2$-h was mainly located in the range of 2−20 nm, peaking at around 5.2 nm. TiO$_2$-0 showed a much lower specific surface area of only 16.0 m^2 g^{-1}; in addition, there was almost no mesopore presented according to its BJH plot. Those results are in good consensus with that observed by TEM. Clearly the creation of mesopores in TiO$_2$-h was closely related to the deep hydrolysis process. Zhong and Song et al. reported highly nanoporous TiO$_2$ spheres prepared by in-situ hydrolysis of titanium glycolate precursor spheres.[26] They proposed that at boiling temperature the titanium glycolate on the surface of spheres would react with water to form a thin titania shell. Because of the different density between the outside titania shell and inner titanium glycolate, the outside thin shell shrank and cracked and then the water went through the cracks and reacted with the inner titanium glycolate, which finally created the nanopores.

Based on the above results and the related available explanation in the literature about the effect of hydrolysis on the pores formation in TiO$_2$ phase, the formation of paper-like film electrode with hierarchical mesoporous structure, prepared by filter paper templating in combination with a following deep hydrolysis treatment, is schematically shown in Figure 7. First, by immersing filter papers into a solution with high concentration of C$_{16}$H$_{36}$O$_4$Ti, some titania source solution was successfully absorbed into the pores and adsorbed onto the surface of the cellulose fibers; thus, the paper morphological shape was easily duplicated. Because the filter papers possessed
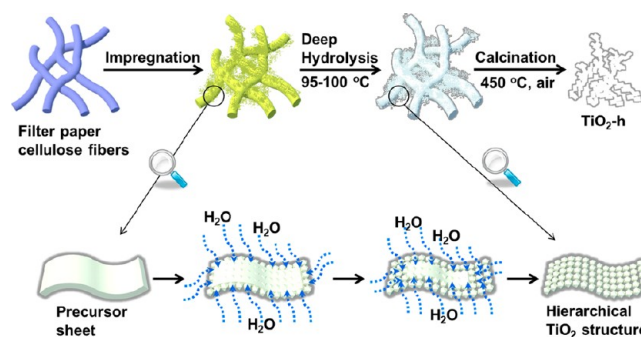

Figure 7. Formation of hierarchical mesoporous TiO$_2$ film through filter paper templating with a following deep hydrolysis treatment.

only large pores with small surface area and considerable amount of $C_{16}H_{36}O_4Ti$ that located at the void space of cellulose belts, the TiO_2 precursor was badly aggregated and the TiO_2 particles were sintered to result in low specific surface area and almost no mesopores after the calcination. The deep hydrolysis treatment allowed the reconstruction of TiO_2 precursor at micro-nanodomain. After the impregnation, there is still void space in the filter paper with $C_{16}H_{36}O_4Ti$ coating. During the deep hydrolysis treatment, water entered the void space and reacted with the solidified tetrbutyl titanate on the surface. In addition, cellulose fibers have also acted as an important network of water channel for well hydrolyzing. Through the two paths, water passed through the whole fiber paper and reacted with tetrbutyl titanate to form a solid film shell. Thin shell shrank and cracked due to the different density between the outside shell and inner tetrbutyl titanate. Then the active water at boiling temperature passed through the cracks and the inner tetrbutyl titanate continued to hydrolyze as shown in Figure 7. The crack and hydrolysis process continued over time, as a result hierarchical mesoporous structure was created and the specific surface area was substantially increased. However, the main paper-like skeleton was remained. As a result, the hierarchical mesoporous TiO_2 structure as shown in Figure 5c was created. Furthermore, we proposed that the homogeneous mesopores in the TiO_2-h as shown in BJH pore size distribution plot is due to the gap of sphere-like titania stacking. A simple model of sphere stacking which our group reported previously was applied to calculate the pore volume for TiO_2-h.[27] Assuming all the nanosized TiO_2 are perfect spheres, they are well packed into 3-D cuboids with dimensions of $A \times B \times C \times d^3$, where A, B, and C are the particle numbers in different directions and d is the particle diameter. The volume of all spheres could be expressed as $A \times B \times C \times (4/3) \times \pi \times (d/2)^3$. The pore volume can be estimated as $[A \times B \times C \times d^3 - A \times B \times C \times (4/3) \times \pi \times (d/2)^3]/[\rho \times A \times B \times C \times (4/3) \times \pi \times (d/2)^3] = \sim 0.23 \text{ cm}^3 \text{ g}^{-1}$, where ρ is the density of TiO_2, 3.89 g cm^{-3}. The calculated specific pore volume is well consistent with the experimental value of ~ 0.26 cm^3 g^{-1}, suggesting the rich mesopores were actually created by the sphere-like titania stacking.

Electrochemical Performance of TiO_2 Film Electrode. Electrochemical performance of the as-fabricated TiO_2-0 and TiO_2-h thin films as lithium intercalation electrodes was first investigated by galvanostatic charge and discharge in half-cell configuration. The disk-shape films, which were cut from template-synthesized TiO_2 papers, as shown as an inset of Figure 8, were directly applied as the working electrodes without any binder or conductive additive. The first discharge/charge curves of the half cells at 0.5 C (84 mA g^{-1}, 1 C = 168 mA g^{-1}) over the potential range of 1.0−3.0 V are presented in Figure 8. The TiO_2-0 electrode showed a reduction plateau voltage of 1.69 V during the first discharge and an oxidation plateau voltage of 1.95 V during the subsequent charge process, while the biphase plateaus voltages of TiO_2-h are 1.72 V/1.92 V during the first discharge/charge processes. The first discharge capacity reached 239 mA h g^{-1} for the TiO_2-h thin film electrode, which is more than 3 times that of the mesopore-free TiO_2-0 electrode (71 mA h g^{-1}). The smaller voltage separation and much higher capacity for the TiO_2-h film electrode than the TiO_2-0 film electrode indicated that the deep hydrolysis treatment greatly improved the electrochemical performance of the thin film TiO_2 electrode, which can be attributed to the reduced lithium ion and electron transport distance owing to
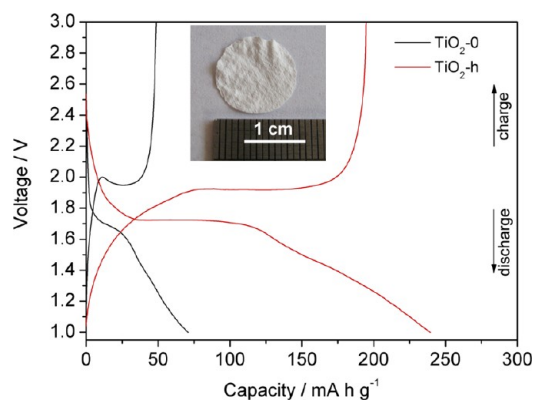

Figure 8. The first charge/discharge curves of the cells with TiO_2-0 (black) and TiO_2-h (red) film electrodes at 0.5 C.

the creation of mesopores and much improved interfacial reaction rate from the greatly increased specific surface area.

The rate performance of TiO_2-h film electrode at different rates was further measured with the results shown in Figure 9.
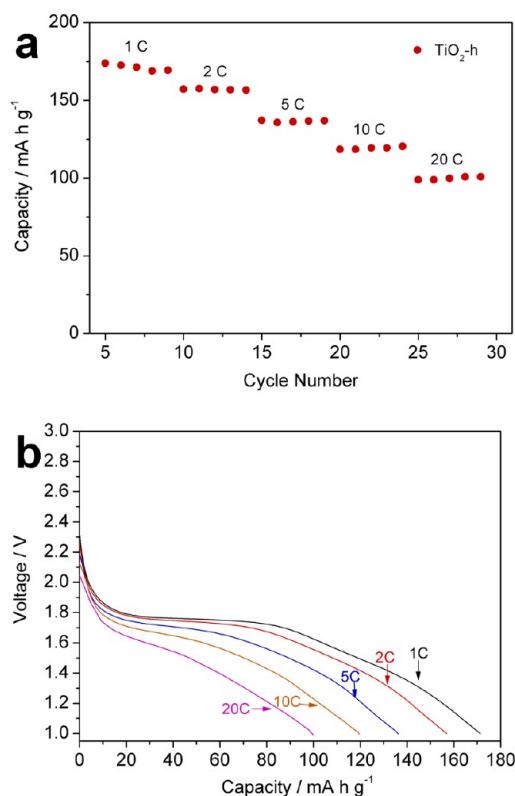

Figure 9. (a) The rate performance and (b) the discharge curves of the cell with TiO_2-h film electrode at different rates (1, 2, 5, 10, and 20 C).

The discharge capacity was 171 mA h g^{-1} at 1 C rate, while the capacity retentions still reached 92, 80, 70, and 58% at the discharge rates of 2, 5, 10, and 20 C, respectively, as compared to that at 1 C rate. Even at a high discharge rate of 20 C, the capacity of the TiO_2-h film electrode still reached around 100 mA h g^{-1}, which is still higher than the initial capacity of TiO_2-0 film electrode at 0.5 C (71 mA h g^{-1}). Such a capacity is highly attractive by thinking the TiO_2-h electrode was composed of 100% active material without any conductive additive and binder.
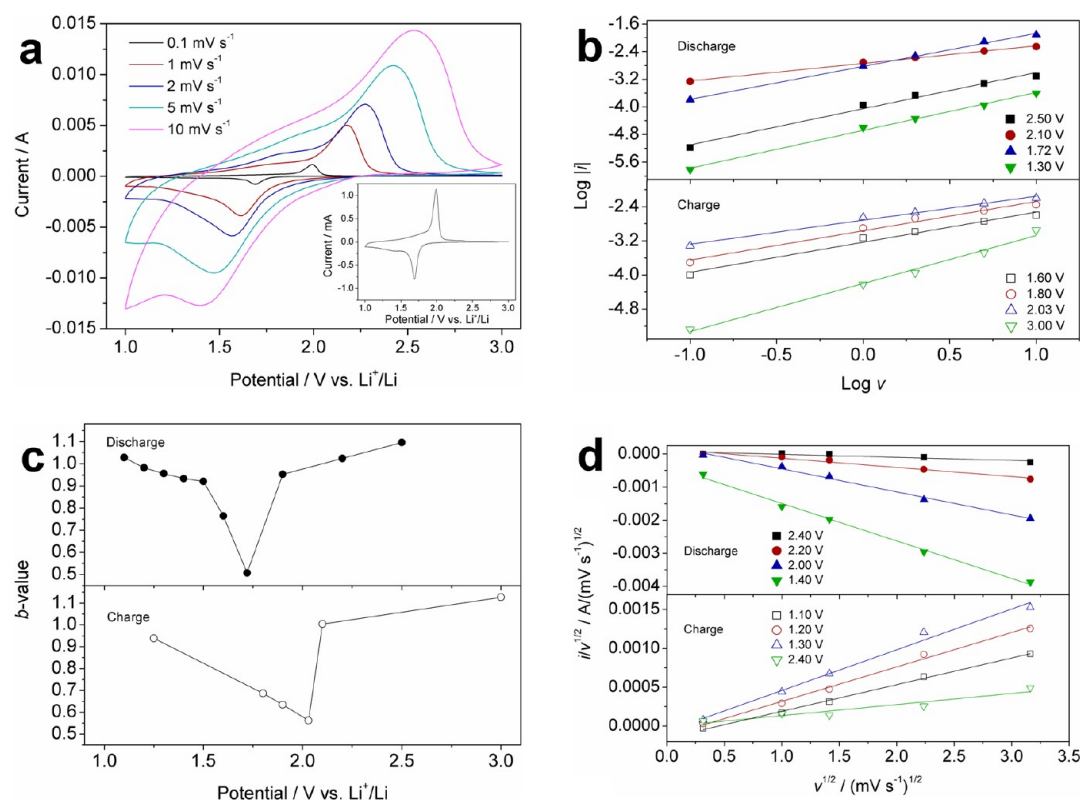
Figure 10. (a) Cyclic voltammograms (CV) at varying sweep rates for TiO_2-h film electrode vs Li^+/Li; the inset shows CV at 0.1 mV s^{-1}. (b) log v–log$|i|$ plots for cathodic (discharge) and anodic (charge) sweeps of CV. (c) Calculated b values for TiO_2-h film electrode as a function of potential for the cathodic and anodic sweep. (d) $v^{1/2}$–$i/v^{1/2}$ plots to calculate k_1 and k_2 at different potentials for TiO_2-h film electrode.

It is recognized recently that potential plateau (1.8−1.7 V) in the discharge curve of anatase TiO_2 was associated with the faradaic lithium insertion reaction, while the slow decay of the voltage at range of 1.7−1.0 V was caused by both faradaic and nonfaradaic capacitive lithium storage on the surface of nanosized TiO_2.[28] As shown in Figure 8, the TiO_2-0 film electrode had an extremely short length of the potential plateau with a capacity of only 53 mA h g^{-1} at the potential range of 1.68−1.0 V, suggesting the sluggish lithium insertion reaction in its bulk phase, while the TiO_2-h film electrode showed high capacity of 123 mA h g^{-1} with the same potential range due to its large surface area. Figure 9b further gives out the discharge curves of the cell with TiO_2-h film electrode at different rates. The length of the potential plateau in the discharge curve became shorter with increasing discharge rate. The plateau was almost completely disappeared at a discharge rate of 20 C while the voltage curve at range of 1.7−1.0 V became a straight line. Such straight line was an indication of a purely capacitive effect. Shin and Maier et al. also observed similar "straight line" nature at high rate for TiO_2 electrode, and they have discussed in detail the mechanisms of bulk intercalation storage and pseudocapacitive storage based on the discharge curves and cycling performance.[29]

To further understand the excellent rate performance of TiO_2-h film electrode, cyclic voltammograms (CV) at various sweep rates were investigated with the curves shown in Figure 10a, and the CV of TiO_2-h film electrode at a sweep rate of 0.1 mV s^{-1}, recorded over a potential window 1.0−3.0 V at room temperature, was specially presented as an inert. The main cathodic and anodic peaks appeared at 1.69 and 1.99 V, respectively, typical for the lithium ion insertion/extraction for

the anatase TiO_2 phase. A pair of weak and wide peaks were also observed at around 1.4/1.8 V, which can be assigned to lithium insertion/extraction for the trace amounts of TiO_2-B phase, as detected by XRD. The currents measured from CVs have three contributions:[30] (1) faradaic reactions of TiO_2/Li_xTiO_2 from the Li^+ insertion/extraction process, (2) faradaic pseudocapacitive lithium storage from the charge transfer process with surface atoms, and (3) lithium storage based on nonfaradaic double layer. Both processes 2 and 3 involve the capacitive effect, which becomes more significant at higher surface area of the electrode.

Although the electrode process is very complex with potential contribution from both the faradaic lithium insertion and capacitive lithium storage, the measured currents typically can be fitted well to the power law, $i = av^b$, where v is the sweep rate and a and b are both adjustable parameters. The b values can be applied to determine the contribution of above different processes to the electrode reaction.[31] Two specific conditions can be defined, $b = 0.5$ and $b = 1$. At $b = 0.5$ the current (i) is proportional to the square root of v, which represents an ideal diffusion limiting process (process 1), while $i = av$ is derived under the condition of $b = 1$, which represents a complete surface limited process (pure capacitive effect, processes 2 and 3). The actual values of b can be determined from the slope of the log $|i|$−log v plots (Figure 10b). The obtained b values at fixed potentials were presented in Figure 10c. At the potential of the peak current during the cathodic (discharge) sweep process, i.e., around 1.72 V, the b value is 0.51, indicating the current is primarily dominated by process 1 under such conditions. At the potential far from the potential of peak current position, the b values were larger than 0.9, suggesting
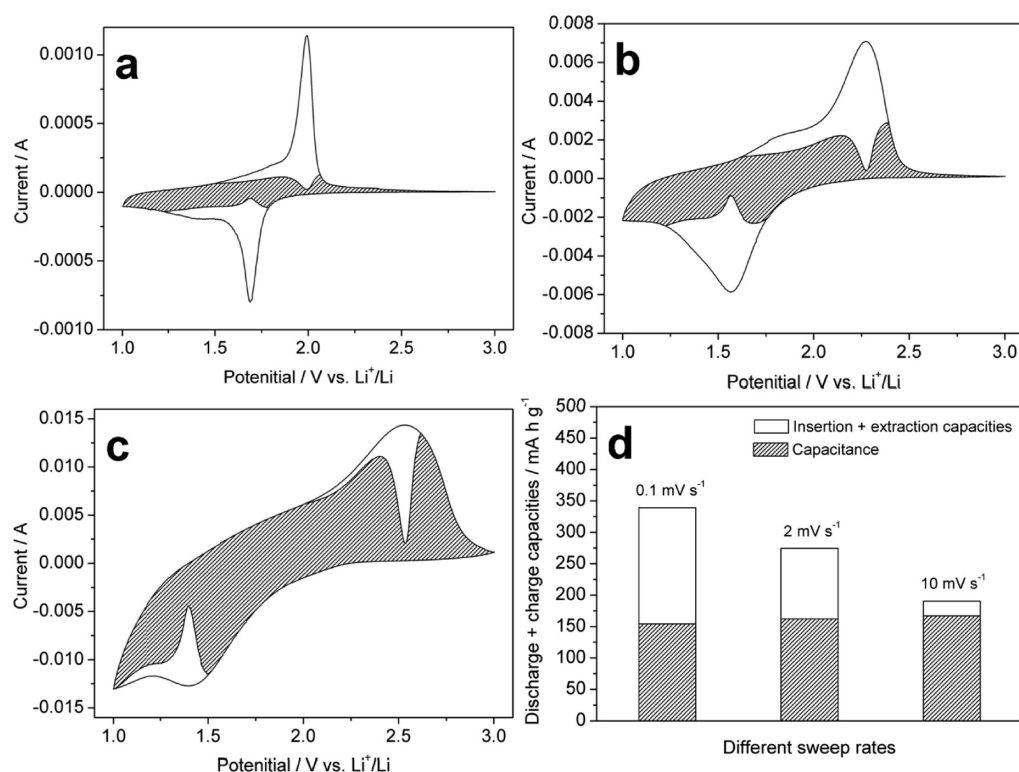
17445

dx.doi.org/10.1021/jp305744c | J. Phys. Chem. C 2012, 116, 17440−17447

Figure 11. Cyclic voltammograms of the cell with TiO_2-h film electrode at sweep rates of (a) 0.1, (b) 2, and (c) 10 mV s^{-1}. (d) Comparison of the lithium insertion/extraction contributions and capacitive contributions to capacities. The total current (solid line in parts a−c) is obtained experimentally. The shaded area is determined by calculation.

the current was dominated mainly by the capacitive effects (processes 2 and 3) under such circumstances. .

At a selected potential, the total measured current is given by the sum of these two parts, which can be written as $i(V) = k_1v + k_2v^{1/2}$, where k_1v and $k_2v^{1/2}$ correspond to the current contributions from the capacitive effects (processes 2 and 3) and Li$^+$ insertion/extraction process (diffusion-limited process 1), respectively. The different contributions can be distinguished quantitatively by determining the values of k_1 and k_2 from the slope and intercept of straight $v^{1/2}-i(V)/v^{1/2}$ plots as shown in Figure 10d. Here, we used the data at scan rate of 0.1 mV s^{-1} to define peak potentials and neglected the slight peak shift at varying sweep rates.[30] Figure 11 shows the respective diffusion-controlled and capacitive contributions in cyclic voltammograms at scan rates of 0.1, 2, and 10 mV s^{-1}. The shaded portions of the CV represent the capacitive contribution, while the other portions correspond to diffusion-controlled (lithium insertion/extraction reaction) contribution. The capacities contributed from faradaic lithium insertion/extraction and capacitive lithium storage is further shown in Figure 11d. With the increase of sweep rate, the absolute value of capacity contributed from faradaic lithium insertion/extraction decreased while it almost remained as a constant for capacitive contribution. This is consistent with the observation from the discharge curves in Figure 9b. At sweep rate of 0.1 mV s^{-1}, the total capacity from discharge and charge processes is 339 mA h g^{-1} (insertion/extraction of 0.5 Li per mole of TiO_2) in which the capacitive contribution reached 46%. However, when the sweep rate increased to 10 mV s^{-1} (around 18 C according to discharge/charge time), the capacitive contribution increased to 88% of the total capacity of 190 mA h g^{-1}, which is in agreement with the disappearance

of potential plateau and straight line nature (1.7−1.0 V) in discharge curve at 20 C (Figure 9b).

High cycling stability is an important issue for the practical application. As shown in Figure 12, good capacity retention and
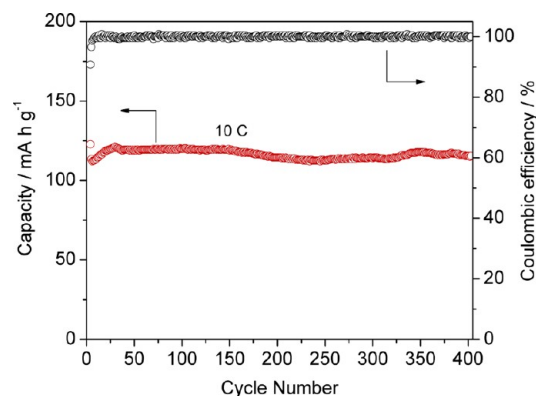

Figure 12. Cycling performance of the cell with TiO_2-h film electrode at 10 C.

Coulombic efficiency of almost 100% was demonstrated through 400 charge−discharge cycles at 10 C rate. It is well-known that TiO_2 may still experience a lattice expansion of about 3% if 1 mol of lithium is inserted into one TiO_2 molecule. Such lattice expansion may cause detrimental effect on the cycling stability of the electrode at fast rate. Based on the above analysis, at high rate actually only a small part of the discharge capacity was contributed from the faradaic lithium insertion for TiO_2-h electrode. In other words, the volumetric change for the TiO_2-h electrode is still small at high charge/discharge rates due to very limited capacity contributed from the faradaic

17446

dx.doi.org/10.1021/jp305744c | J. Phys. Chem. C 2012, 116, 17440−17447

lithium intercalation. In addition, the hierarchical mesoporous structure also played an important role in the stable cycling performance due to reducing mechanical lattice strain by accommodating the cell expansion during the lithium ion insertion/extraction process. As a result, a high cycling stability was observed even at fast charge/discharge rate.

CONCLUSIONS

In summary, hierarchical mesoporous TiO_2 paper-like thin films were successfully fabricated by facile filter paper templating in combination with a following deep hydrolysis treatment. The film electrode, without applying any conductive agent, exhibited attractive performance with initial capacity of 239 mA h g^{-1} and superior capacity of 100 mA h g^{-1} at 20 C. In addition, we found that the capacitive effects contributed 88% at sweep rate of 10 mV s^{-1}, indicating that such hierarchical mesoporous TiO_2 film electrode is absolutely suitable for fast and reversible lithium storage which showed high cycling stability at 10 C through 400 cycles. As a general method, we believe that this facile method is also applicable to synthesize other thin-film materials with hierarchical mesoporous structure. Because of the abundance and renewability of cellulose, the current technique is economically highly attractive and easy for scale-up. It may find potential applications in many fields.

AUTHOR INFORMATION

Corresponding Author

*Tel +86 25 83172256, fax +86 25 83172242, e-mail shaozp@njut.edu.cn.

Notes

The authors declare no competing financial interest.

ACKNOWLEDGMENTS

REFERENCES

(1) Tarascon, J. M.; Armand, M. *Nature* **2001**, *414*, 359−367.

(2) Armstrong, A. R.; Armstrong, G.; Canales, J.; Garcia, R.; Bruce, P. G. *Adv. Mater.* **2005**, *17*, 862−865.

(3) Wang, D. H.; Choi, D. W.; Li, J.; Yang, Z. G.; Nie, Z. M.; Kou, R.; Hu, D. H.; Wang, C. M.; Saraf, L. V.; Zhang, J. G.; et al. *ACS Nano* **2009**, *3*, 907−914.

(4) Hu, Y. S.; Kienle, L.; Guo, Y. G.; Maier, J. *Adv. Mater.* **2006**, *18*, 1421−1426.

(5) Arico, A. S.; Bruce, P.; Scrosati, B.; Tarascon, J. M.; Van Schalkwijk, W. *Nat. Mater.* **2005**, *4*, 366−377.

(6) Bruce, P. G.; Scrosati, B.; Tarascon, J. M. *Angew. Chem., Int. Ed.* **2008**, *47*, 2930−2946.

(7) Huczko, A. *Appl. Phys. A: Mater. Sci. Process.* **2000**, *70*, 365−376.

(8) van Bommel, K. J. C.; Friggeri, A.; Shinkai, S. *Angew. Chem., Int. Ed.* **2003**, *42*, 980−999.

(9) Braun, E.; Eichen, Y.; Sivan, U.; Ben-Yoseph, G. *Nature* **1998**, *391*, 775−778.

(10) Thurn-Albrecht, T.; Schotter, J.; Kastle, C. A.; Emley, N.; Shibauchi, T.; Krusin-Elbaum, L.; Guarini, K.; Black, C. T.; Tuominen, M. T.; Russell, T. P. *Science* **2000**, *290*, 2126−2129.

(11) Cheng, F. Y.; Tao, Z. L.; Liang, J.; Chen, J. *Chem. Mater.* **2008**, *20*, 667−681.

(12) Li, X. X.; Cheng, F. Y.; Guo, B.; Chen, J. *J. Phys. Chem. B* **2005**, *109*, 14017−14024.

(13) Needham, S. A.; Wang, G. X.; Liu, H. K. *J. Power Sources* **2006**, *159*, 254−257.

(14) Zhou, H. S.; Zhu, S. M.; Hibino, M.; Honma, I.; Ichihara, M. *Adv. Mater.* **2003**, *15*, 2107−2111.

(15) Fan, J.; Wang, T.; Yu, C. Z.; Tu, B.; Jiang, Z. Y.; Zhao, D. Y. *Adv. Mater.* **2004**, *16*, 1432−1436.

(16) Kavan, L.; Attia, A.; Lenzmann, F.; Elder, S. H.; Gratzel, M. *J. Electrochem. Soc.* **2000**, *147*, 2897−2902.

(17) Liu, L.; Li, Y.; Yuan, S. M.; Ge, M.; Ren, M. M.; Sun, C. S.; Zhou, Z. *J. Phys. Chem. C* **2010**, *114*, 251−255.

(18) Brezesinski, T.; Wang, J.; Polleux, J.; Dunn, B.; Tolbert, S. H. *J. Am. Chem. Soc.* **2009**, *131*, 1802−1809.

(19) Nam, K. T.; Kim, D. W.; Yoo, P. J.; Chiang, C. Y.; Meethong, N.; Hammond, P. T.; Chiang, Y. M.; Belcher, A. M. *Science* **2006**, *312*, 885−888.

(20) Raja, M. W.; Mahanty, S.; Basu, R. N. *J. Mater. Chem.* **2009**, *19*, 6161−6166.

(21) Huang, J. G.; Kunitake, T. *J. Am. Chem. Soc.* **2003**, *125*, 11834−11835.

(22) Huang, J.; Matsunaga, N.; Shimanoe, K.; Yamazoe, N.; Kunitake, T. *Chem. Mater.* **2005**, *17*, 3513−3518.

(23) Wang, B.; Han, N.; Meng, D.; Yue, R. L.; Yan, J. H.; Chen, Y. F. *Particuology* **2011**, *9*, 253−259.

(24) Sun, Y.; Hu, X.; Yu, J. C.; Li, Q.; Luo, W.; Yuan, L.; Zhang, W.; Huang, Y. *Energy Environ. Sci.* **2011**, *4*, 2870−2877.

(25) Yuan, T.; Zhao, B. T.; Cai, R.; Zhou, Y. K.; Shao, Z. P. *J. Mater. Chem.* **2011**, *21*, 15041−15048.

(26) Zhong, L. S.; Hu, J. S.; Wan, L. J.; Song, W. G. *Chem. Commun.* **2008**, 1184−1186.

(27) Wang, J.; Zhou, Y. K.; Hu, Y. Y.; O'Hayre, R.; Shao, Z. P. *J. Phys. Chem. C* **2011**, *115*, 2529−2536.

(28) Myung, S. T.; Takahashi, N.; Komaba, S.; Yoon, C. S.; Sun, Y. K.; Amine, K.; Yashiro, H. *Adv. Funct. Mater.* **2011**, *21*, 3231−3241.

(29) Shin, J. Y.; Samuelis, D.; Maier, J. *Adv. Funct. Mater.* **2011**, *21*, 3464−3472.

(30) Wang, J.; Polleux, J.; Lim, J.; Dunn, B. *J. Phys. Chem. C* **2007**, *111*, 14925−14931.

(31) Lindstrom, H.; Sodergren, S.; Solbrand, A.; Rensmo, H.; Hjelm, J.; Hagfeldt, A.; Lindquist, S. E. *J. Phys. Chem. B* **1997**, *101*, 7717−7722.

17447

dx.doi.org/10.1021/jp305744c | *J. Phys. Chem. C* 2012, 116, 17440−17447